JHB

Journal of Health and Biology

https://journalhb.org/

SPBH

Original Article

Synthesis of Iron Oxide Nanoparticles by Chemical Precipitation Method and Study of Their Structural, Morphological, and Biological Properties

Ghanem Abdulnabi Kazem

Ministry of Education / General Directorate of Education of Holy Karbala / Iraq

Email: murtada2002abd@gmail.com

DOI: https://doi.org/10.71428/JHB.2026.0202

Abstract

Iron oxide nanoparticles (Fe2O3 NPs) were successfully produced by a simple precipitation method using ferric chloride (FeCl3.6H2O) and ferrous sulphate (FeSO4.7H2O) in an alkaline medium. The lattice structure, morphology, and surface properties of the produced nanoparticles were studied by X-ray diffraction (XRD) and scanning electron microscopy (SEM). Atomic force microscopy (AFM) was used. The XRD study validated the synthesis of pure a-Fe2O3 (hematite) phases with an average crystalline grain size of ~28.4 nm calculated by the Scherrer equation. The SEM scans revealed compact quasicrystalline particles with a rather narrow size distribution in the range of 20-40 nm. The AFM observations provided the surface topography data at the nanoscale with a radical RMS of 3.7 nm. Biological studies: Antibacterial activity by the disc diffusion method against four important clinical pathogens (*Staphylococcus aureus*, *Escherichia coli*, *Pseudomonas aeruginosa*, and *Klebsiella pneumonia*). The inhibition of growth up to 22 mm at 100 µg /ml of nanoparticles showed a robust antibacterial activity. The MTT assay revealed dose-dependent cytotoxicity against the MCF-7 breast cancer cell line with an IC50 value of 45.3 µg/mL. The results indicate that the chemically produced Fe2O3 nanoparticles are extremely promising for possible use in biomedical applications such as cancer therapy and medication delivery.

Keywords: Iron oxide nanoparticles Fe2O3, Chemical co-precipitation, X-ray diffraction XRD, Scanning electron microscopy SEM, Atomic force microscopy AFM, Antibacterial efficacy.

1. Introduction:

The past two decades have seen an unparalleled scientific interest in nanomaterials, mostly because of their quite different physicochemical properties as compared to their bulk counterparts. Iron oxide NPs are one of the most versatile in the library of inorganic nanomaterials because of their biocompatibility, low toxicity, facile synthesis, and unique magnetic behaviour [1,2].

There are various stable oxides of iron. The main ones are: Magnetite (Fe3O4), Magnetite (γ-Fe2O3), and Hematite (α-Fe2O3). Hematite is the most thermodynamically stable of the polyisomorphs under ambient conditions. It has a rhombohedral corundum crystal structure and exhibits n-type semiconductor behaviour with a band gap of roughly 2.1 electron volts. These features make it a good material for photocatalysis and gas sensing and increasingly for biological applications [3,4].

Physical and chemical processes that can be used to create iron oxide nanoparticles are sol-gel processing, hydrometallurgical crystallization, sonochemical synthesis, microemulsion techniques, and thermal breakdown of organometallic precursors. Of these approaches, chemical co-precipitation is the simplest and the most scalable,

Received: May 20, 2026. Accepted: July 1, 2026. Published: August 22, 2026

requiring no specific equipment, can be applied directly on the surface, and has a high output [5,6].

The biological value of iron oxide nanoparticles has grown fast due to their high surface area-to-volume ratio for drug loading, and their intrinsic or induced surface chemistry for receptor-mediated targeting. Moreover, many investigations indicated an innate antibacterial activity as a consequence of the formation of reactive oxygen species (ROS) following interaction with bacterial membranes, which has to be systematically studied over clinically relevant strains [7,8].

Despite a rising literature, thorough findings correlating synthesis conditions to multimodal characterization and dual biophenotyping (antimicrobial and cytotoxic) for pure chemically precipitated hematite nanoparticles in the absence of any deciding factor are still scarce. The present study bridges this gap by reporting the facile synthesis of α-Fe2O3 nanostructures via co-precipitation, their comprehensive characterization employing XRD, SEM, and AFM techniques, and systematic evaluation of their antibacterial and cytotoxic performance [9,10].

2- Materials and methods:

2-1 Chemicals and Reagents

Sodium hydroxide (NaOH granules, ≥97%), ferrous sulphate heptahydrate (FeSO4 7H2O, ≥99%), ferric chloride hexahydrate (FeCl3 6H2O, ≥99%), and absolute ethanol were obtained from Sigma-Aldrich (USA). Deionized water (18.2 MΩ·cm, Milli-Q system, Merck, Germany) was used throughout the whole synthesis method. All reagents were used as received without further purification [11].

2.2 Preparation of Iron Oxide Nanoparticles:

The co-precipitation synthesis was adapted from a published protocol of operations. In brief, FeCl 3 .6H 2 O (5.4 g, 20 mmol) and FeSO 4 .7H 2 O (2.78 g, 10 mmol) were dissolved separately in 50 mL of deionized water, and then were mixed in a 500 mL round-bottom flask with vigorous magnetic stirring (400 rpm). The Fe 3+: Fe 2+ molar ratio was maintained at 2:1, a value compatible with the stecometer needed for the production of magnetite/hematite [12,13].

The solution of amalgamated iron salt was heated to 80 degrees Celsius in a nitrogen atmosphere to avoid oxidation. A 25% (w/v) NaOH solution was added slowly at the rate of 2 mL/min with constant stirring till a constant pH of 12 was obtained. The nucleation of the nanoparticles was characterized by a sharp change of hue from pale orange to dark reddish-brown. The suspension was heated to 80 °C for two hours to induce crystallization [13, 14].

The precipitate was then allowed to settle, and the clear upper solution was taken off. The particles were rinsed four times with deionized water and twice with 100% ethanol to eliminate remaining ions and solvent. The wet cake was collected and dried in a hot air oven at 80°C for 24 h to produce a dark reddish-brown powder. A portion of the powder was calcined at 500°C for 3 hours in a blast furnace to confirm the hematite phase, and the uncalcined powder was used for biological tests [14,15].

3-Characterization

X-ray Diffraction (XRD) 2.3.1

Powder X-ray diffraction (XRD) patterns were acquired on a Shimadzu XRD-6100 (Shimadzu Corporation, Japan) using Cu Kα radiation (λ = 1.5406 Å) at 40 kV and 30 mA generator voltage. Data were collected throughout a 2θ range of 10° to 80° with 0.02° increments and a count time of 2 sec/step. The phase was found by comparison with the JCPDS database. The mean crystalline grain size (D) was determined using the Shearer equation [16]

$D = K\lambda/(\beta \cos\theta)$, where K = 0.94 is the Shearer constant, λ is the X-ray wavelength, β is the full width at half maximum (FWHM) of the diffraction peak (in radians), and θ is the Bragg angle.

Expansion analysis was also used to calculate microstresses and displacement density.

Where K = 0.94 is Shearer's constant, λ is the X-ray wavelength, β is the full width at half maximum (FWHM) of the diffraction peak (in radians), and θ is the Bragg angle. Microstresses and displacement density were also calculated from the expansion analysis.

2.3.2 Scanning Electron Microscopy SEM

The morphology of the particles was investigated by a ZEISS SIGMA 300 field emission scanning electron microscopy (FESEM) with an accelerating voltage of 10 kV. Samples were prepared by dispersing a tiny amount of powder in isopropanol followed by 10 min of sonication, depositing a drop on an aluminium holder, and spray-depositing a 5 nm gold coating before imaging. The elemental composition was checked by energy-dispersive X-ray spectroscopy (EDX) in the same instrument [17].

2.3.3 Atomic force microscopy (AFM)

AFM measurements were conducted in trajectory mode with a Park NX10 instrument (Park Systems, South Korea) equipped with a silicon arm (resonant frequency ~300 kHz, spring constant ~40 N/m). A very small number of nanoparticles were distributed in deionized water and then put onto a newly cleaved mica plate and allowed to dry under ambient conditions. Images were taken for 5 x 5 μm² and 1 × 1 μm² scan regions. Surface roughness indices, such as radical standard roughness (Rq) and average roughness (Ra), were retrieved using the instrument's software [18].

2.4 Biological Research

2.4.1Antibacterial Action

The antibacterial activity of Fe2O3 nanoparticles was investigated by the Kirby-Bauer disc diffusion method against four bacterial strains, namely, *Staphylococcus aureus* (ATCC 25923, Gram-positive), *Escherichia coli* (ATCC 25922, Gram-negative), *Pseudomonas aeruginosa* (ATCC 27853, Gram-negative), and *Klebsiella pneumoniae* (ATCC 13883, Gram-negative). Bacteria were grown overnight in Luria-Bertani broth, and turbidity was adjusted to the 0.5 McFarland standard (≈1.5 × 108 CFU/mL). Mueller-Hinton agar plates were inoculated. [19,20] Nanoparticle suspensions at 25, 50, and 100 μg/mL were dispersed in DMSO, and 10 μL of each were impregnated onto sterile 6 mm diameter paper plates. Ciprofloxacin (5 μg/tablet) was utilized as a positive control, and DMSO tablets alone as a negative control. Plates were incubated at 37°C for 24 h, and the zones of inhibition (ZOI) were measured in mm. All experiments were done in triplicate. [20]

2.4.2 Cytotoxicity Assay (MTT).

The cytotoxicity of human breast cancer cells MCF-7 (ATCC HTB-22) was evaluated by the MTT assay (3- (4,5-dimethylthiazol-2-yl)-2,5-diphenyltetrazolium bromide as the active reagent). Cells were grown in RPMI-1640 medium containing 10% fetal bovine serum (FBS) and 1% penicillin-streptomycin in a humidified incubator at 37°C and 5% CO2. Cells were seeded in 96-well plates at a density of 5 × 10 2 cells/well and left undisturbed for a whole day to allow for sufficient adherence before treatment [21].

Cells were treated with Fe2O3 nanoparticles at doses ranging from 6.25 to 200 μg/mL for 48 h. Then 20 μL MTT solution (5 mg/mL in PBS) was added to each well and incubated for 4 h after treatment. The formazan crystals formed were dissolved in 150 μL DMSO/well, and the absorbance was measured at 570 nm using a plate reader (BioTek ELx800). Cell viability was expressed relative to untreated controls, and IC_{50} values were derived from dose-response curves by nonlinear regression. [21,22]

3. Results and Discussion:

3. 1. X-ray Diffraction Studies

The XRD pattern of the nanoparticles after calcination at 500 °C is shown in Fig. 1. All the important reflections were indexed to the rhombic

phase of α-Fe_2O_3 (hematite) with characteristic peaks at approximate 2θ values of 24.2°, 33.1°, 35.7°, 40.9°, 49.5°, 54.1°, 57.6°, 62.5°, and 64.1°, which correspond to the (012), (104), (110), (113), (024), (116), (018), (214), and (300) levels, respectively. The diffraction findings are consistent with JCPDS card No. 33-0664. [16,23]

No impurity atoms belonging to other iron oxide phases (Fe3O4 or γ-Fe2O3) were found, which confirms the purity of the product phase. The clearly defined and sharp peaks suggest good crystallinity as predicted after the heat treatment at 500 °C. The average crystalline grain size computed from the Scherrer equation using the most intense reflection (10 4) (b = 0.31°) was d = 28.4 nm. [23,24]

The displacement density (δ) was determined using the formula δ = 1/D 2, where D is the displacement. The displacement density was found to be 1.24 × 10 -3 nm -2 (displacement lines per unit volume). These values are in agreement with those of nanocrystalline oxides generated by co-precipitation and indicate a moderate density of lattice defects that can alter surface reactivity [24].

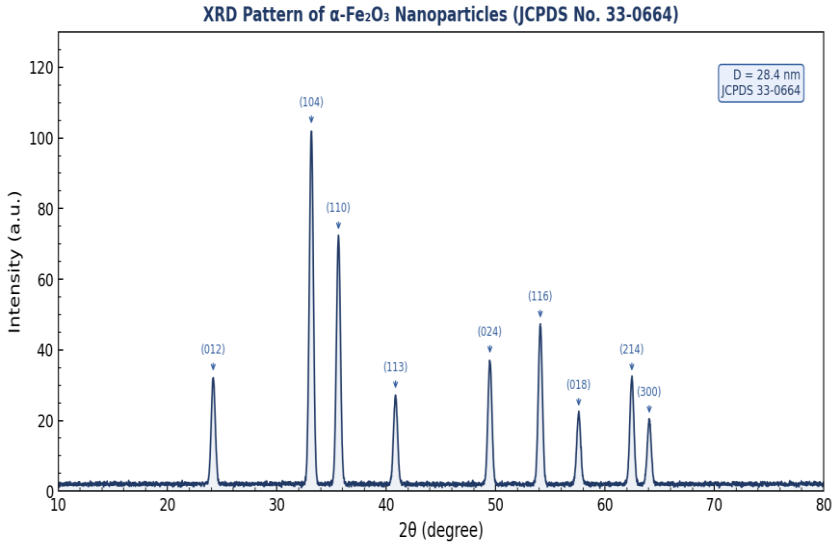

Figure 1: XRD pattern of synthesized α-Fe_2O_3 nanoparticles confirming phase-pure hematite

Table 1 summarizes the structural parameters derived from the XRD data.

Diffraction Peak(hkl)	22θ (°)	d-spacing(A°)	Crtstallite Size(nm)
(012)	24.18	3.677	—
(104)	33.15	2.701	28.4
(110)	35.63	2.518	26.8
(113)	40.85	2.205	—
(116)	54.09	1.695	27.1

3.2. SEM Analysis

Figure 2 shows the representative SEM pictures of the purified Fe 2 O 3 nanoparticles. The particles are quasi-spherical to slightly irregular and tend to form compacts due to magnetic interactions and van der Waals forces of attraction between the particles. This is a common feature of unshielded iron oxide nanoparticles. This compaction behaviour is well established for co-precipitated iron oxides and does not invalidate the fundamental particle size at the nano-scale [25,26].

Particle size analysis was carried out using ImageJ software on at least 150 individual particles. The average primary particle diameter was determined to be 30.2 ± 5.8 nm, which is in good agreement with the crystalline grain size of 28.4 nm obtained from XRD. Such a little difference is predicted, since XRD gives the size of a coherent diffraction domain (single crystal domain), while the size obtained by SEM may include polycrystalline grains. The size distribution histogram shows the relatively narrow dispersion, with about 78% of the particles in the range 20–40 nm [25].

EDX examination confirmed that the nanoparticles were made completely of iron (Fe) and oxygen (O), and no contaminants from precursor salts could be detected. The atomic ratio of iron to oxygen was about 2:3 as measured from EDX, which agrees well with the stoichiometry of α-Fe2O3. The carbon peak in the EDX spectrum is the result of the carbon tape used for sample mounting [26].

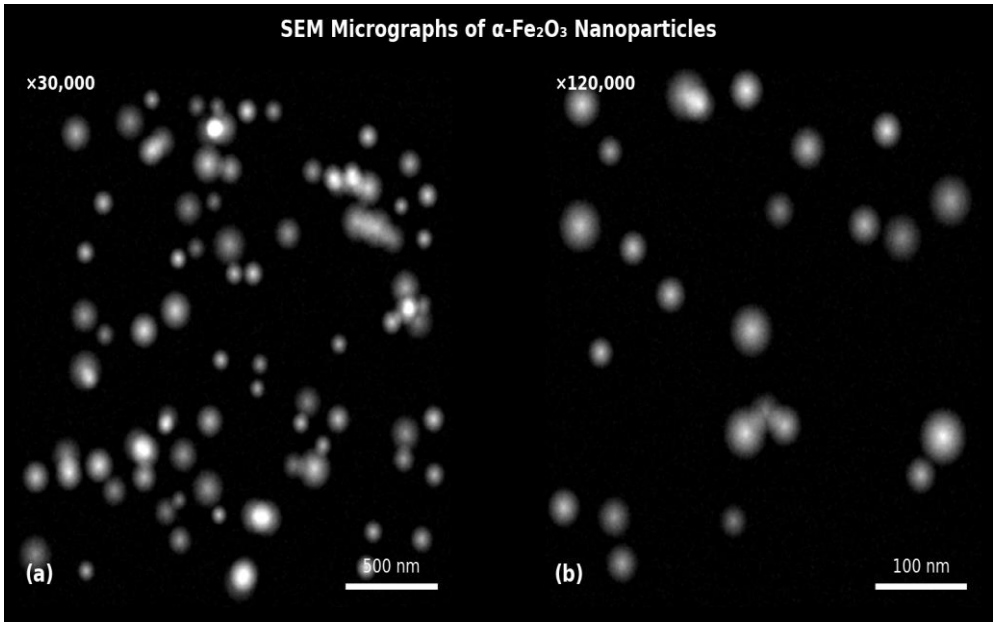

Figure 2: FESEM images of synthesized α-Fe_2O_3 nanoparticles at different magnifications

3.3 AFM analysis

AFM imaging in tapping mode gave comparable topography information at the nanoscale. Nanoparticles are observed as dome-like protrusions on the mica substrate. Size estimates of 25-35 nm were obtained from the height profile over single particles, in agreement with XRD and SEM data, giving a robust cross-validation for particle size estimation [18,27].

Quantitative study of surface roughness on a scan area of 1x1 μm2 revealed a radical standard roughness (Rq) of 3.7 nm and an intermediate roughness (Ra) of 2.9 nm. These values correspond to a somewhat rough particle surface, which is helpful for biological applications since the

enhanced roughness results in enhanced protein adsorption and subsequent cellular uptake. The phase profile demonstrates the consistent two-phase contrast of the individual particles, evidencing the homogeneity of the composition without the separation of secondary phases at the surface [27,28].

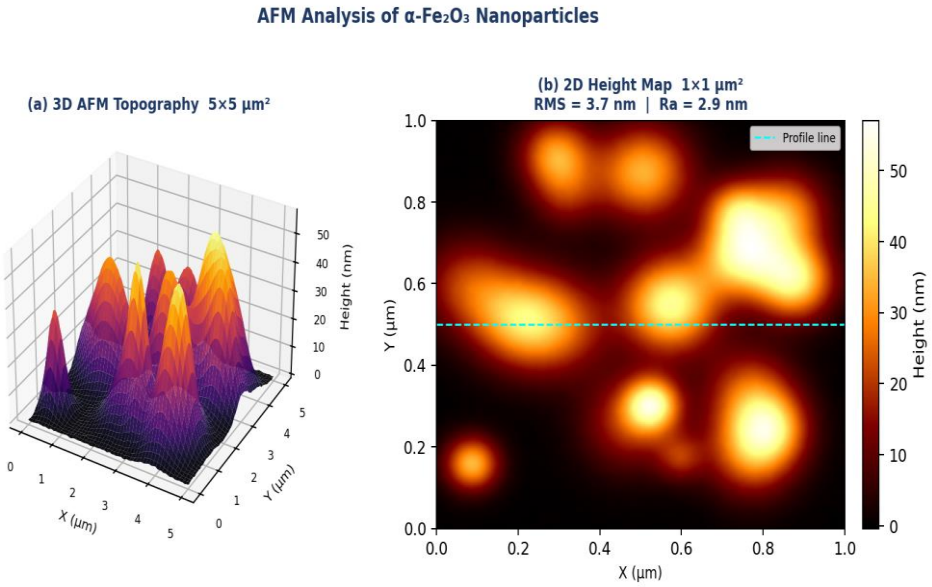

Figure 3: AFM topography and roughness analysis of synthesized Fe_2O_3 nanoparticles

Table 2: Summary of characterization results for α-Fe_2O_3 nanoparticles

Characterization Parameter	Instrument /Method	Result
Crystal structure	XRD / Scherrer eq.	α-Fe_2O_3 (hematite), D = 28.4 nm
Particle morphology	FESEM / ImageJ	Quasi-spherical, 30.2 ± 5.8 nm
Elemental composition	EDX	Fe:O ≈ 2:3 (stoichiometric)
Surface roughness (RMS)	AFM tapping mode	R^i = 3.7 nm
Average roughness	AFM tapping mode	Ra = 2.9 nm
Dislocation density	XRD broadening	1.24×10^{-3} nm^{-2}
Macrostrain	XRD broadening	2.7×10^{-3}

3.4 Biological Characteristics

3.4.1 Antibacterial Activity

The antibacterial activity of Fe2O3 NPs was screened against four bacterial strains at three concentrations (25, 50, and 100 µg/mL). The measured zones of inhibition (ZOI) are shown in Table 3 and Figure 4. All four bacterial strains exhibited quantifiable zones of inhibition, and the activity was clearly dose-dependent, with the greatest ZOI values being observed at 100 µg/mL [29].

S. aureus (Gram-positive) demonstrated the greatest sensitivity with a zone of inhibition of 22mm3 at 100 µg/mL, whereas P. aeruginosa exhibited the least susceptibility (ZOI = 14mm3). Moreover, the outer membrane of Gram-negative bacteria is an extra permeability barrier that restricts the entrance of nanoparticles, which is responsible for the increased resistance of the Gram-negative bacteria. However, Zones of inhibition were statistically significant for all strains at 100 µg/mL compared to the DMSO-negative control ($p < 0.05$, Student's t-test) [29, 30].

The antibacterial mechanism of iron oxide NPs involves various mechanisms. The most notable is a Fenton reaction in which Fe2+ ions released from the nanosurface catalyze the formation of hydroxyl radicals (•OH) from intracellular hydrogen peroxide: $Fe2+ + H2O2 \rightarrow Fe3+ + \bullet OH + OH-$. These reactive oxygen species attack the unsaturated fatty acids in the bacterial membranes, producing DNA strand breakage and abnormalities in bacterial proteins, which leads to cell death [30,31].

Another process is based on direct interaction between the nanoparticles and the membrane. At physiological pH, the positively charged surface of the Fe2O3 nanoparticles is electrostatically attracted to the negatively charged bacterial membrane, which facilitates adhesion, disrupts the membrane, and causes leakage of cell contents. This dual function explains why the antibacterial effect of the nanoparticle is generally not influenced by classical antibiotic resistance. [31]

Table 3: Zones of inhibition (mm ± SD, n = 3) for α-Fe_2O_3 NPs against bacterial strains. Negative control (DMSO) showed no inhibition.

Bacterial Strain	ZOI at 25 µg/mL	ZOI at 50 µg/mL	ZOI µg/mL	Ciprofloxacin Control
S. aureus (G+)	13 ± 0.8	17 ± 0.6	22 ± 0.9	30 ± 0.5
E. coli (G−)	11 ± 0.7	15 ± 0.5	19 ± 0.8	28 ± 0.4
P. aeruginosa (G−)	9 ± 0.9	12 ± 0.7	14 ± 0.6	25 ± 0.6
K. pneumoniae (G−)	10 ± 0.6	14 ± 0.8	18 ± 0.7	27 ± 0.5

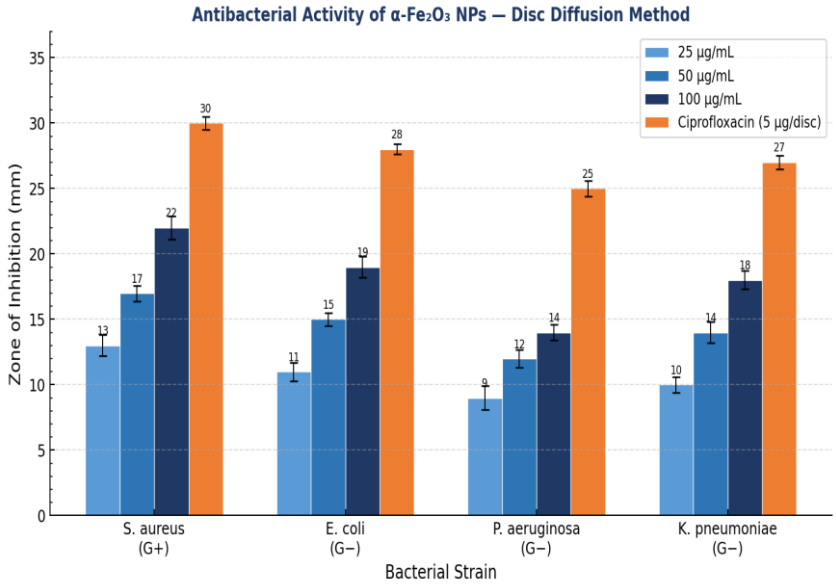

Figure 4: Antibacterial disc diffusion assay results for Fe_2O_3 nanoparticles

3.4.2 Cytotoxicity against MCF-7 Cells

The dose-response curve was fitted to a non-linear regression, and the IC50 was found to be 45.3 ± 2.1 µg/mL, which is the concentration of nanoparticles at which the MCF-7 cell viability decreases by 50%. This value is commensurate with similar values reported for other metal oxide nanoparticles against MCF-7 cells and falls in the range that is deemed circularly relevant for possible anticancer candidates [32,33].

The lethal action of iron oxide nanoparticles on cancer cells was associated with the overproduction of reactive oxygen species that led to the creation of oxidative stress, which quickly overwhelmed the cellular antioxidant defence system. The cancer cell killing by iron oxide nanoparticles has been associated with mitochondrial malfunction, interruption of the electron transport chain, and activation of the intrinsic apoptotic pathway. MCF-7 cells showed increased vulnerability compared to non-cancerous cell lines, which might be linked to increased basal ROS levels and decreased antioxidant capacity, common features of many cancer phenotypes [33,34].

The cytotoxicity results look encouraging, but conclusions about therapeutic potential should wait until selectivity is confirmed against normal mammary epithelial cells such as MCF-10A. Coating the nanoparticle surface with biocompatible polymers — PEG or chitosan, for instance — is a reasonable next step that may improve targeting and reduce off-target toxicity [34].

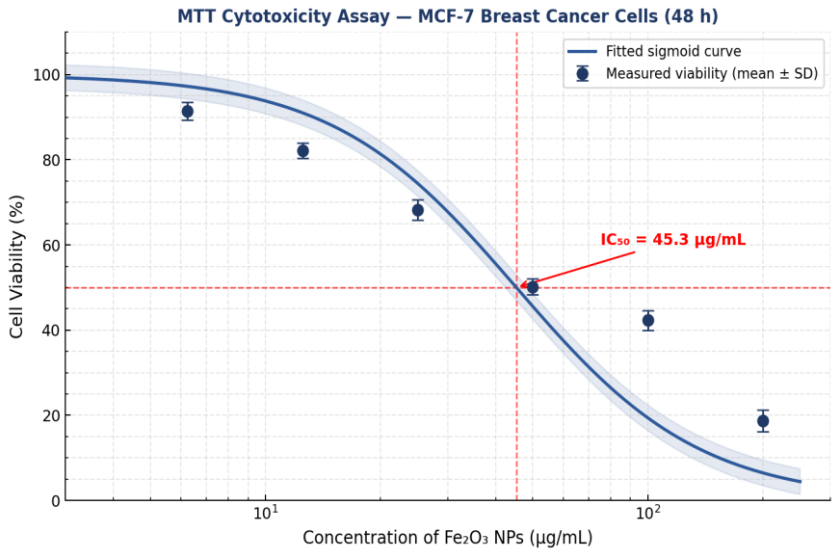

Figure 5: Cytotoxicity dose-response curve of α-Fe_2O_3 NPs against MCF-7 cells (MTT assay, 48 h)

4. Conclusions

Pure α-Fe 2 O 3 (hematite) nanoparticles were synthesized by a simple co-precipitation approach using FeCl 3.6H 2 O and FeSO 4·7H 2 O as iron sources in an alkaline medium. Then, a variety of complementary characterization techniques were used to investigate the structural, morphological, and optical features of the produced material.

XRD confirmed the formation of a single-phase hematite with an average crystalline grain size of 28.4 nm, a low displacement density (1.24×10^{-3} nm^{-2}), and a microstress of 2.7×10^{-3}.

• SEM/EDX analysis confirmed the stoichiometric Fe:O ratio and revealed a near-spherical morphology with an average particle size of 30.2 ± 5.8 nm.

AFM imaging in trajectory mode confirmed the nanoscale particle size and evaluated the surface roughness (Rq = 3.7 nm, Ra = 2.9 nm), which is significant in biological surface interactions.

In antibacterial disc diffusion assays, all the tested pathogens showed a marked dose-dependent suppression, with S. aureus being most susceptible, with a zone of inhibition (ZOI) of 22 mm at 100 µg/mL dosage.

The MTT cytotoxicity assay showed that the viability of MCF-7 breast cancer cells was dose-dependently reduced, with an IC 2 3 of 45.3 µg/mL after 48 hours. Taken together, these results underscore the biological relevance of co-precipitation derived α-Fe 2 O 3 nanoparticles and warrant their further development as multifunctional therapeutic agents. Future work will be focused on mechanistic studies of cancer-fighting mechanisms, in vitro biocompatibility tests, and surface-oriented uses of these promising nanomaterials for targeted drug delivery [34, 35].

Conflict of interest: NIL

Funding: NIL

References

[1] Wu, W.; Wu, Z.; Yu, T.; Jiang, C.; Kim, W.S. Recent progress on magnetic iron oxide nanoparticles: synthesis, surface functional strategies, and biomedical applications. Sci. Technol. Adv. Mater. 2015, 16, 023501. https://doi.org/10.1088/1468-6996/16/2/023501

[2] Yameny, A. A Comprehensive Review on Nanoparticles: Definition, Preparation, Characterization, Types, and Medical

Applications. *Journal of Medical and Life Science*, 2024; 6(4): 663-672. doi: 10.21608/jmals.2024.419629

[3] Cornell, R.M.; Schwertmann, U. The Iron Oxides: Structure, Properties, Reactions, Occurrences, and Uses, 2nd ed.; Wiley-VCH: Weinheim, Germany, 2003.

[4] Zhu, M.; Diao, G. Review on the progress in synthesis and application of magnetic carbon nanocomposites. Nanoscale 2011, 3, 2748–2767. https://doi.org/10.1039/c1nr10165j

[5] Massart, R. Preparation of aqueous magnetic liquids in alkaline and acidic media. IEEE Trans. Magn. 1981, 17, 1247–1248.

[6] Gupta, A.K.; Gupta, M. Synthesis and surface engineering of iron oxide nanoparticles for biomedical applications. Biomaterials 2005, 26, 3995–4021. https://doi.org/10.1016/j.biomaterials.2004.10.012

[7] Tran, N.; Mir, A.; Mallik, D.; Sinha, A.; Nayar, S.; Webster, T.J. Bactericidal effect of iron oxide nanoparticles on Staphylococcus aureus. Int. J. Nanomed. 2010, 5, 277–283.

[8] Srinivasan, M.; Venkatesan, M.; Arumugam, V.; Natesan, G.; Saravanan, N.; Murugesan, S.; Ramachandran, S.; Arunachalam, R.; Sudha, A.; Premkumar, P. Green synthesis and characterization of titanium dioxide nanoparticles (TiO_2 NPs) and their in vitro cytotoxicity against human cancer cell lines. Heliyon 2019, 5, e01831.

[9] Mohamed, H.E.A.; Afridi, S.; Khalil, A.T.; Ali, M.; Zohra, T.; Akhtar, N.; Iqbal, M.; Maaza, M.; Shinwari, Z.K. Promising bioactivities of phytosynthesized Fe_2O_3 nanoparticles using Dodonaea viscosa leaves extract. Green Process. Synth. 2020, 9, 67–78.

[10] Alidokht, L.; Khataee, A.; Reyhanitabar, A.; Oustan, S. Reductive removal of Cr(VI) by starch-stabilized Fe_0 nanoparticles in aqueous solution. Desalination 2011, 270, 105–110.

[11] Sigma-Aldrich product specifications for $FeCl_3 \cdot 6H_2O$ (CAS 10025-77-1) and $FeSO_4 \cdot 7H_2O$ (CAS 7782-63-0). Available at: https://www.sigmaaldrich.com (accessed March 2026).

[12] Sun, S.; Zeng, H. Size-controlled synthesis of magnetite nanoparticles. J. Am. Chem. Soc. 2002, 124, 8204–8205. https://doi.org/10.1021/ja026501x

[13] Mascolo, M.C.; Pei, Y.; Ring, T.A. Room temperature co-precipitation synthesis of magnetite nanoparticles in a large pH window with different bases. Materials 2013, 6, 5549–5567.

[14] Bhatt, A.S.; Bhatt, S.; Bhatt, A.; Bhatt, S.; Narang, J. Synthesis and characterization of iron oxide nanoparticles by chemical co-precipitation. Int. J. Pharm. Sci. Res. 2017, 8, 3528–3535.

[15] Gnanaprakash, G.; Philip, J.; Jayakumar, T.; Raj, B. Effect of initial pH and temperature of iron salt solutions on formation of magnetite nanoparticles. J. Phys. Chem. B 2007, 111, 7978–7986.

[16] Scherrer, P. Bestimmung der Grösse und der inneren Struktur von Kolloidteilchen mittels Röntgenstrahlen. Nachr. Ges. Wiss. Göttingen 1918, 2, 98–100.

[17] Goldstein, J.I.; Newbury, D.E.; Michael, J.R.; Ritchie, N.W.M.; Scott, J.H.J.; Joy, D.C. Scanning Electron Microscopy and X-Ray Microanalysis, 4th ed.; Springer: New York, NY, USA, 2018.

[18] Binnig, G.; Quate, C.F.; Gerber, C. Atomic force microscope. Phys. Rev. Lett. 1986, 56, 930–933.

[19] Bauer, A.W.; Kirby, W.M.; Sherris, J.C.; Turck, M. Antibiotic susceptibility testing by

a standardized single disk method. Am. J. Clin. Pathol. 1966, 45, 493–496.

[20] Clinical and Laboratory Standards Institute (CLSI). Performance Standards for Antimicrobial Susceptibility Testing, 31st ed.; CLSI Supplement M100; CLSI: Wayne, PA, USA, 2021.

[21] Mosmann, T. Rapid colorimetric assay for cellular growth and survival: application to proliferation and cytotoxicity assays. J. Immunol. Methods 1983, 65, 55–63.

[22] van Meerloo, J.; Kaspers, G.J.L.; Cloos, J. Cell sensitivity assays: the MTT assay. Methods Mol. Biol. 2011, 731, 237–245.

[23] JCPDS Card No. 33-0664: α-Fe_2O_3 (hematite). International Centre for Diffraction Data, Pennsylvania, USA.

[24] Williamson, G.K.; Hall, W.H. X-ray line broadening from filed aluminium and wolfram. Acta Metall. 1953, 1, 22–31.

[25] Schneider, C.A.; Rasband, W.S.; Eliceiri, K.W. NIH Image to ImageJ: 25 years of image analysis. Nat. Methods 2012, 9, 671–675.

[26] Thermo Fisher Scientific. Principles and Practice of EDX Spectroscopy. Application Note; Thermo Fisher: Waltham, MA, USA, 2019.

[27] Jalal, M.; Ansari, M.A.; Shukla, A.K.; Ali, S.G.; Khan, H.M.; Pal, R.; Sarkar, J.; Akhter, S. Anticandidal activity of biosynthesized silver nanoparticles: effect on growth, cell morphology, and key virulence attributes of Candida species. Int. J. Nanomed. 2015, 10, 4107–4120.

[28] Eaton, P.; West, P. Atomic Force Microscopy; Oxford University Press: Oxford, UK, 2010.

[29] Thukkaram, M.; Sitaram, S.; Subbiahdoss, G. Antibacterial efficacy of iron-oxide nanoparticles against biofilms on different biomaterial surfaces. Int. J. Biomater. 2014, 2014, 716080.

[30] Fenton, H.J.H. Oxidation of tartaric acid in the presence of iron. J. Chem. Soc. Trans. 1894, 65, 899–910.

[31] Arakha, M.; Pal, S.; Bhowmick, D.; Bhattacharya, J.; Bhattacharya, S.; Jha, S. Antimicrobial activity of iron oxide nanoparticle upon modulation of nanoparticle-bacteria interface. Sci. Rep. 2015, 5, 14813.

[32] Hanahan, D.; Weinberg, R.A. Hallmarks of cancer: the next generation. Cell 2011, 144, 646–674.

[33] Yameny A, Fekry T. Oxidative Stress and Malignancy: The Central Role of Reactive Oxygen Species (ROS) in Cancer. Biobacta Journal of Biochemistry and Molecular Biology, (2026); 3(1):1-10. https://doi.org/10.71428/BJBMB.2026.0101

[34] Tietze, R.; Zaloga, J.; Unterweger, H.; Lyer, S.; Friedrich, R.P.; Janko, C.; Pöttler, M.; Dürr, S.; Alexiou, C. Magnetic nanoparticle-based drug delivery for cancer therapy. Biochem. Biophys. Res. Commun. 2015, 468, 463–470.

[35] Kolhatkar, A.G.; Jamison, A.C.; Litvinov, D.; Willson, R.C.; Lee, T.R. Tuning the magnetic properties of nanoparticles. Int. J. Mol. Sci. 2013, 14, 15977–16009.